Nano Research

ISSN 1998-0124 CN 11-5974/O4
https://doi.org/10.1007/s12274-022-4976-0

Research Article

Introducing B–N unit boosts photocatalytic H_2O_2 production on metal-free g-C_3N_4 nanosheets

Weikang Wang[1,2,§], Wei Zhang[3,§], Yueji Cai[1], Qing Wang[1], Juan Deng[1], Jingsheng Chen[1], Zhifeng Jiang[3], Yizhou Zhang[4] (✉), and Chao Yu[1] (✉)

[1] *School of Environmental and Chemical Engineering, Jiangsu University of Science and Technology, Zhenjiang, 212100, China*
[2] *School of Materials Science and Engineering, Jiangsu University, Zhenjiang 212013, China*
[3] *Institute for Energy Research, Jiangsu University, Zhenjiang 212013, China*
[4] *School of Chemistry and Materials Science Institute of Advanced Materials and Flexible Electronics (IAMFE), Nanjing University of Information Science and Technology, Nanjing 210044, China*
[§] *Weikang Wang and Wei Zhang contributed equally to this work.*

Received: 28 June 2022 / **Revised:** 26 August 2022 / **Accepted:** 27 August 2022

ABSTRACT

Metal-free catalyst for photocatalytic production of H_2O_2 is highly desirable with the long-term vision of artificial photosynthesis of solar fuel. In particular, the specific chemical bonds for selective H_2O_2 photosynthesis via $2e^-$ oxygen reduction reactions (ORR) remain to be explored for understanding the forming mechanism of active sites. Herein, we report a facile doping method to introduce boron-nitrogen (B–N) bonds into the structure of g-C_3N_4 nanosheets (denoted as BCNNS) to provide significant photocatalytic activity, selectivity and stability. The theoretical calculation and experimental results reveal that the electron-deficient B–N units serving as electron acceptors improve photogenerated charge separation and transfer. The units are also proved to be superior active sites for selective O_2 adsorption and activation, reducing the energy barrier for *OOH formation, and thereby enabling an efficient $2e^-$ ORR pathway to H_2O_2. Consequently, with only bare loss of activity during repeated cycles, the optimal H_2O_2 production rate by BCNNS photocatalysts reaches 1.16 mmol·L^{-1}·h^{-1} under LED_{365nm} irradiation, increasing nearly 2~5 times as against the state-of-art metal-free photocatalysts. This work gives the first example of applying B–N bonds to enhance the photocatalytic H_2O_2 production as well as unveiling the underlying reaction pathway for efficient solar-energy transformations.

KEYWORDS

g-C_3N_4 nanosheets, metal-free photocatalyst, B–N bonds, oxygen reduction reaction, H_2O_2 production

1 Introduction

Hydrogen peroxide (H_2O_2) is one of TOP 100 chemicals with widespread applications in bleaching, semiconductor manufacturing, chemical synthesis, and even employed as an alternative energy carrier [1, 2]. Artificial photosynthesis has emerged as a greener and eco-friendly approach for H_2O_2 production, due to its advantages of safety, efficiency and no pollution output as compared with the conventional anthraquinone oxidation process [1]. Driven by sustainable solar energy, photocatalysts that promote O_2 reduction reaction (ORR) and water oxidation with photogenerated electrons can be used to synthesize H_2O_2 [3, 4]. As for water oxidation pathway to directly synthesize H_2O_2, the two-electron water oxidization ($2H_2O + 2h^+ \rightarrow H_2O_2 + 2H^+$) by photogenerated holes is thermodynamically unfavorable, due to the higher oxidation potential (+1.78 eV *vs.* NHE) than that of four-electron water oxidation to form O_2 (+1.23 eV *vs.* NHE) [5–7]. Thus, developing highly active and selective $2e^-$ ORR catalysts that are composed of inexpensive and earth-abundant elements is the prerequisite of this direct reaction route [8–10]. To date, numerous promising $2e^-$ ORR catalysts candidates have stood out for H_2O_2 photosynthesis, in particular, polymeric carbon nitride (C_3N_4) based composites catalysts [11, 12]. As a typical 2-dimentional (2D) polymer semiconductor, the graphitic carbon nitride (g-C_3N_4) possesses advantages of visible-light response, suitable band structure, easy scalable-synthesis, excellent thermal stability and chemical stability, endowing it with practical long-term application potential [13, 14]. Although great progress has been achieved [15], the ORR activation of C_3N_4 is still retarded and the intrinsic low kinetics of the reaction are associated with rapid photogenerated charge recombination and poor selective O_2 adsorption [3].

The introduction of specific chemical bonds to materials is now generally believed to alert the electron arrangements and promote the charge separation for reactions carried out in fuel cells [16–18], which is very promising to meet the surge in demand of high-efficiency H_2O_2 production photocatalyst. At present, the introduction of boron (B) atoms into carbon-based matrixes have been theoretically predicted and verified by experiments that can act as superior adsorption or activation sites for inert N_2, CO_2 and CO [19–21]. In addition, Wang et al. demonstrated that *in-situ* formed B–C bonds contribute to a direct and continuous

Address correspondence to Chao Yu, chao_yu@just.edu.cn; Yizhou Zhang, Yizhou.zhang@nuist.edu.cn

electrochemical generation of H_2O_2 with high selectivity (reaching 95%) and high H_2O_2 partial currents [22]. It is proposed that the presence of B could create new catalytic active sites without affecting surface π-electron distributions on carbon-based catalysts. More importantly, the organic semiconductors with B–N coordinate bonds (B⇐N) have been proven to act as electron acceptors in organic solar cells [23, 24].

Here we introduced electron-deficient building blocks of B–N bonds into the s-triazine framework based g-C_3N_4, significantly promoting the photogenerated charge separation and transfer. A rational design of B–N units modified g-C_3N_4 nanosheets (BCNNS) was achieved by B-atoms doping and they are capable of yielding H_2O_2 at an impressive rate of 1.16 mmol·L^{-1}·h^{-1} under 365 nm-monochrome light emitting diode (LED_{365nm}) irradiation with only bare loss of activity during repeated cycles, surpassing most of the state-of-art photocatalysts. The structural characterizations revealed that the B–N units successfully constructed in g-C_3N_4 framework, which can be regarded as electron acceptors. Meanwhile, as an electron-deficient building block, B–N units in g-C_3N_4 framework can act as adsorption and activation sites for O_2 molecules, contributing to an enhanced H_2O_2 production performance. This B–N modified catalyst also shows excellent stability by maintaining over 90% in continuous five cycles. Furthermore, the optical/electrochemical measurements indicated that the electron donor-acceptor (D-A) pairs induced by B–N bonds in conjugated polymers (g-C_3N_4) can finely tune their band gaps to realize an enhanced visible light-harvesting. More available electrons can be trapped and participate in surface reactions because of the accelerated photogenerated charge separation and transfer. The comparison of photocatalytic H_2O_2 formation and decomposition rates, time-resolved photoluminescence decay (TRPD) and ORR measurements analysis provided strong evidences for the improved H_2O_2 production kinetics and strong O_2 adsorption and activation on BCNNS photocatalyst. More importantly, the density functional theory (DFT) theoretical and electron spin resonance (ESR) spectroscopy analysis demonstrated that H_2O_2 is produced via a selective $2e^-$ ORR pathway by BCNNS with a significant reduced energy barrier of *OOH-intermediates formation. This work would bring new insights in settling two key issues of O_2 activation and photogenerated charge transfer to achieve efficient $2e^-$ ORR process for photocatalytic H_2O_2 production.

2 Results and discussion

In this work, a boron (B)-doped g-C_3N_4 nanosheets (BCNNS) photocatalyst was synthesized through a facile thermal treatment followed by ultrasound-assisted exfoliation and vacuum freeze-drying approach. The proposed reaction route and atomic diagram of final product are schematically illustrated in Scheme 1. For comparison, the bulk g-C_3N_4 (CN) and g-C_3N_4 nanosheets (CNNS) without B-doping were also fabricated. The microstructure morphologies of CN, CNNS and BCNNS were characterized by the scanning electron microscope (SEM) and transmission electron microscope (TEM). Obviously, CN displays a layer-stacked agglomerates morphology in Fig. 1(a), while after ultrasound-assisted exfoliation, the resultant CNNS reveals much thinner nanosheets with more nanoscale pores in Fig. 1(b). Interestingly, as can be seen from Fig. 1(c), the BCNNS possesses more loose structure with large pores, meaning more edge active sites on thin nanosheets. Accordingly, the elemental mapping images in Fig. 1(d) indicate the uniform distribution of C, N and B over BCNNS, suggesting the successful fabrication of B-doped g-C_3N_4. Moreover, their corresponding SEM images are provided in Fig. S1 in the Electronic Supplementary Material (ESM).

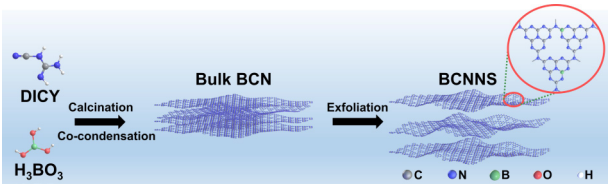

Scheme 1 Diagram of preparation process for BCNNS photocatalyst.

The corresponding powder X-ray diffraction (XRD) patterns of prepared samples are revealed in Fig. 1(e). Compared with that of CN sample, the intensity of both two diffraction peaks at 13.1° (100) and 27.7° (002) for CNNS reduce obviously [25]. Similarly, the two distinct diffraction peaks nearly disappear in the XRD pattern of BCNNS, and only a weak broad peak appears near 27.7°, suggesting the loss of long-range order in the in-plane atomic arrangements in BCNNS sample due to the B-atom doping. In addition, Fig. S2 (in the ESM) illustrates the Fourier-transform infrared (FT-IR) spectra of all three samples. Clearly, all spectra display three main absorption regions at 3,600–3,200 cm^{-1} (–OH or N–H band), 1,600–1,200 cm^{-1} (CN heterocycles) and 806 cm^{-1} (tri-s-triazine units), indicating that the tri-s-triazine-based structure of g-C_3N_4 is remained for all prepared samples during the H_3BO_3-incroporated thermal treatment, ultrasound-assisted exfoliation and vacuum freeze-drying process. Furthermore, there is an obvious IR signal at 930 cm^{-1} for B–O appearing in the plot of BCNNS, mainly ascribed to edge B-OH sites, while several peaks at 1382 and 798 cm^{-1} corresponding to B–N are overlapped by IR absorption peaks of g-C_3N_4 intrinsic framework [25, 26]. More importantly, compared with those of CN and CNNS, obvious peaks around 3,420 and 3,180 cm^{-1} of –OH and N–H groups can be detected in the FTIR spectra of BCNNS, endowing the prepared samples with hydrophilicity [26].

Furthermore, the nitrogen (N_2) adsorption–desorption isotherms of all prepared were detected to clarify their pore structure. In Fig. 1(f), all tested samples demonstrate type IV isotherm with H3-type hysteresis loop, illustrating their mesoporous characteristics [27]. Compared with those of CN and CNNS samples, the pore diameter distribution curve (inset of Fig. 1(f)) of BCNNS exhibits highest mesoporous content in region of 10 –50 nm, agreed well with TEM results. As expected, the BCN exhibits largest specific surface area of 182 $m^2·g^{-1}$ than those of CNNS (123 $m^2·g^{-1}$) and CN (52 $m^2·g^{-1}$). It is obvious that the porous structure and large specific surface area of BCNNS result in more catalytic active sites and promote mass transport for high-efficiency photocatalysis.

To confirm the successful doping of B-atoms in g-C_3N_4 frameworks, we further performed the X-ray photoelectron spectroscopy (XPS), and ^{13}C and ^{11}B solid-state magic-angle spinning nuclear magnetic resonance (SSMAS NMR) characterizations. The surface XPS full spectra of CN, CNNS and BCNNS sample are shown in Fig. S3(a) in the ESM). All three measured samples contain C, N and O elements, while B element can be only detected in BCNNS with a B-doping content of 8.8 wt.%. In Fig. 2(a) of the high-resolution C 1s spectrum for BCNNS, no binding energy peak centered at around 283.0 eV derived from B–C bonds can be found [28], signifying that no N atoms were replaced by B-atoms doping. In comparison with that of CNNS, the intensity of peak at 284.8 eV for BCNNS raises notably, associating with carbon contaminants from the ambience and sp^2 hybridized carbon atoms (C–C). Moreover, a new peak at 286.2 eV assigned to C–O bond appears in BCNNS [29], derived from the introduction of H_3BO_3 precursor. Figure 2(b) reveals the high-resolution N 1s spectra of CNNS and BCNNS. An additional binding energy peak centered at 398.1 eV can be monitored for

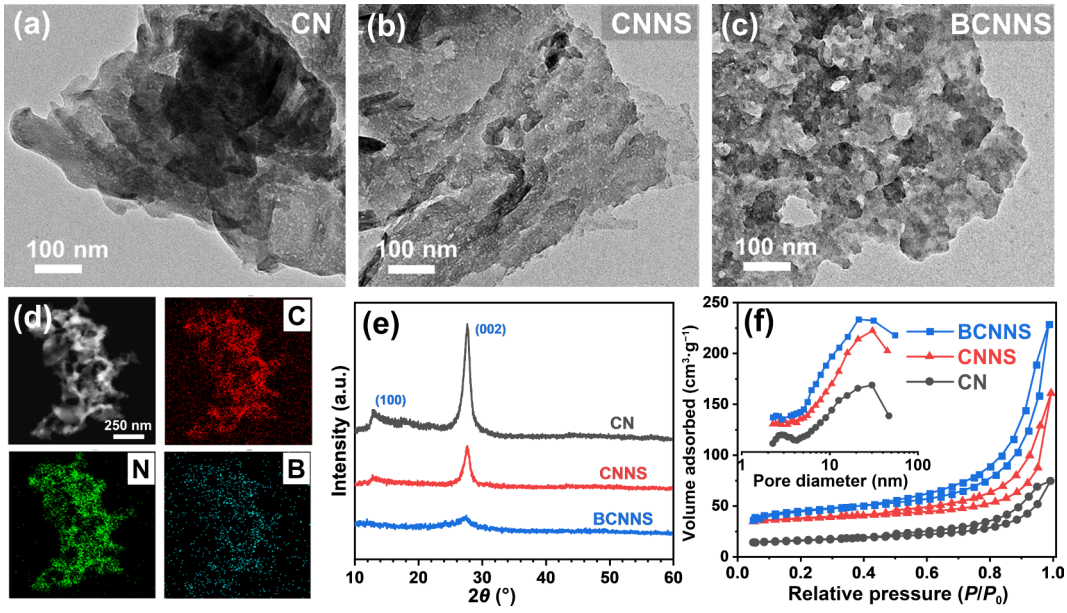

Figure 1 (a)–(c) TEM images of CN, CNNS and BCNNS. (d) TEM image of BCNNS and corresponding element mapping images of C, N and B. (e) XRD patterns and (f) N_2 adsorption-desorption isotherms and corresponding pore size distribution curves (inset) of CN, CNNS and BCNNS.

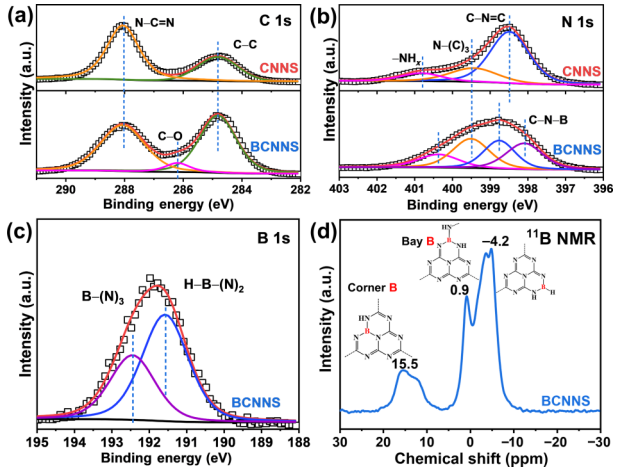

Figure 2 High-resolution (a) C 1s and (b) N 1s XPS spectra of CNNS and BCNNS. High-resolution (c) B 1s spectra and (d) ^{11}B SSMAS NMR spectra of BCNNS (insets in d of the inferred g-C_3N_4 unit with different B doping sites).

BCNNS, ascribed to C–N–B bonds [28]. In addition, the observed binding energies from CNNS and BCNNS corresponding to the bi-coordinated N (C–N=C) are 398.5 and 398.8 eV, respectively. The increased binding energy of C–N=C in BCNNS is mainly due to the electrophilic property induced by B-atom doping [25, 30]. Meaningfully, compared with that of CNNS, the peak area ratio of bi-coordinated and tri-coordinated N atoms (N–$(C)_3$) in the N 1s spectra of BCNNS reduces remarkably, which could be ascribed to that some of C–N=C bonds converts to C–N–B bonds due to the B-atoms doping. Additionally, the enhanced intensity of binding energies peak derived from amino nitrogen (–NH_x) for BCNNS agrees well with the FT-IR result (Fig. S2 in the ESM), conductive to promoting hydrophilicity of photocatalyst.

As can be seen from Fig. S3(b) of high-resolution O 1s spectrum, three binding energy peaks can be found at 533.2, 532.0 and 531.1 eV, corresponding to –OH, adsorbed H_2O and C–O species, respectively [17]. Apparently, the intensity of all peaks for BCNNS is higher than that of CNNS, mainly owing to the introduction of H_3BO_3 precursor and ultrasound-assisted exfoliation treatment in water. In addition, the binding energy peaks in high-resolution B 1s spectrum of BCN are mainly concentrated at 192.4 and 191.6 eV (Fig. 2(c)), resulting in the formed B–$(N)_3$ and –N_2BH bonds, respectively.

Figure S3(c) in the ESM and Fig. 2(d) illustrate the solid-state ^{13}C and ^{11}B MAS NMR spectroscopy, respectively. As shown in the ^{13}C NMR spectra, the plots of BCNNS is very similar to that of tri-s-triazine-based g-C_3N_4 framework in CNNS [29]. This verifies that the tri-s-triazine units of g-C_3N_4 materials are remained in BCNNS, coincided with the FT-IR result. More importantly, the ^{11}B NMR spectrum of BCNNS reveals a dominant signal peak at a chemical shift of –0.42 ppm, along with a shoulder peak at 0.9 ppm, and a board one at 15.5 ppm, attributed to the B-doping in the bay-(including sp^3-coordinated borane such as –N_2BH) and corner-carbon sites (inset of Fig. 2(d)) of tri-s-triazine units in g-C_3N_4 [31]. Meaningfully, no B–C or B–B signal peak can be detected in solid-state ^{11}B NMR spectrum, as well as in the XPS analysis, indicating the incorporated B atoms dispersed atomically in the g-C_3N_4 framework to form B–N–C coordination (Scheme 1). The obtained B–N–C coordination possibly plays key role as electron acceptors for boosting the photogenerated charge transfer, and active sites for O_2 activation and reduction reaction [23, 24].

The optical properties and corresponding band structure of prepared photocatalysts were systematically investigated through UV-vis diffuse reflectance spectra (DRS), XPS valence band spectra and Mott-Schottky (M-S) plots. In Fig. 3(a), the UV–visible (350–850 nm) absorption spectra reveal a slight blue shift of the intrinsic absorption edge in the exfoliated BCNNS and CNNS with respect to CN sample, ascribed to their thinner nanosheet feature. The derived bandgaps from the plots (Fig. S4(a) in the ESM) estimated by Kubelka-Munk (K-M) equation are 2.77, 2.89 and 2.8 eV for CN, CNNS and BCNNS, respectively [32]. Figure S4(b) in the ESM illustrates the XPS valence band spectra of prepared photocatalysts, demonstrating same valence band edge energy (1.56 eV) for both CN and CNNS. Meaningfully, the VB maximum increased to 1.86 eV for BCNNS, owing to the p-type doping of B-atoms [32, 33]. The Mott-Schottky (M-S) plots within frequencies ranging from 1.5 to 3.2 kHz were subsequently conducted to identify the conductivity types and flat band potential of prepared samples. As shown in Figs. S4(c)–S4(e) in the ESM), the obtained positive slopes prove that all three photocatalysts are typical n-type semiconductors. The determined flat band potentials from the x-intercepts in the corresponding M-S

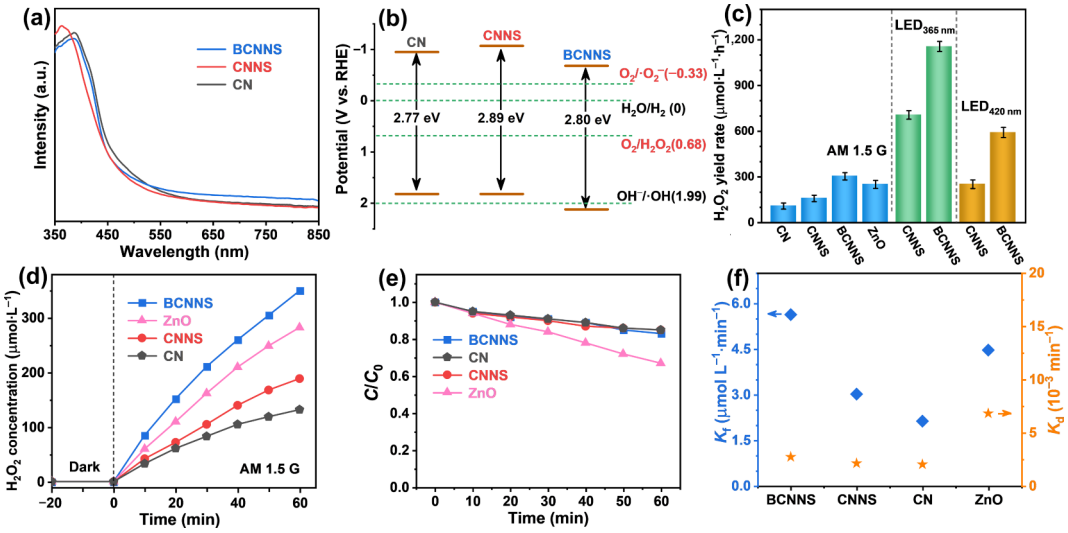

Figure 3 (a) UV–vis DRS and (b) corresponding band structure of CN, CNNS and BCNNS. (c) Photocatalytic H_2O_2 yield rate of prepared samples under different irradiation. (d) Time-dependent curves of photocatalytic H_2O_2 formation under simulated sunlight (AM 1.5 G, 100 mW·cm^{-2}) in 1 h, (e) Time-dependent curves of photocatalytic H_2O_2 decomposition (C_0 = 2 mmol·L^{-1}) and (f) K_f and K_d constant of ZnO, CN, CNNS and BCNNS samples.

plots for CN, CNNS and BCNNS are –1.55, –1.60 and –1.39 eV (versus the saturated Ag/AgCl reference electrode at pH = 6.4), respectively. The band structure versus reversible hydrogen electrode (RHE) of obtained samples is consequently shown in Fig. 3(b) [34].

The photocatalytic H_2O_2 production rate by obtained g-C_3N_4-based photocatalysts were thereafter measured under different irradiation (simulated sunlight and LED monochrome light source) with isopropanol (IPA) as hole sacrificial agent. The yielded H_2O_2 was determined by iodometry colorimetric method [1], and the calibration curve is illustrated in Fig. S5 in the ESM.

A series of B-doped carbon nitride (BCN) photocatalysts with different doping content were synthesized (Figs. S6(a) and S6(b) in the ESM), and evaluated under simulated sunlight (AM 1.5 G, 100 mW·cm^{-2}) irradiation, in comparison with commercial boron nitride (BN). As shown in Fig. S6(c) of the ESM, the H_2O_2 production rate of optimal photocatalyst of 0.5-BCN achieved 255 μmol·L^{-1}·h^{-1}. To further improving the photocatalytic activity for H_2O_2

production, the BCNNS was obtained by the ultrasound-assisted exfoliation and vacuum freeze-drying treatments on 0.5-BCN. As expected, in Fig. 3(c), the H_2O_2 production activity of BCNNS with thinner nanosheet structure grew even higher, reaching 304 μmol·L^{-1}·h^{-1}, nearly three times larger than that of pristine CN sample (109 μmol·L^{-1}·h^{-1}). Meanwhile, the photocatalytic activity of commercial ZnO photocatalyst was tested (251 μmol·L^{-1}·h^{-1}) as a comparison. Especially, under LED monochrome light source (365 and 420 nm, 200 mW·cm^{-2}), photocatalytic activity of BCNNS increases dramatically, achieving a highest H_2O_2 production rate of 1.16 mmol·L^{-1}·h^{-1} (LED_{365nm}). This brilliant performance comparable to that of other reported metal-free and some metal-based photocatalysts (Table S1 in the ESM).

The pondus hydrogenii (pH) effect of reaction solution and the catalyst dosage effect on photocatalytic efficiency were performed and shown in Figs. S7(a) and S7(b) in the ESM. As revealed in Fig. S7(a) in the ESM, the acidic condition of reaction solution is beneficial to H_2O_2 generation, owing to the proton coupled electron transfer (PCET) mechanism in ORR process [16], which would be limited by alkaline environment. Figure S7(b) in the ESM indicates that the H_2O_2 yield rate was enhanced with the catalyst dosage increasing. The scale-up photocatalytic test over BCNNS with gram-scale dosage was also carried out (Fig. S7(c) in the ESM). With 1 g of BCNNS photocatalyst in 1 L of 10% IPA reaction solution, the H_2O_2 yield rate reaches 523 μmol·L^{-1}·h^{-1} in 3 hours under simulated sunlight irradiation (AM 1.5 G, 100 mW·cm^{-2}). The produced H_2O_2 amount by 1 g of BCNNS was much higher than that of BCNNS with milligram-scale, indicating the application potential in industrial production. Meanwhile, BCNNS also revealed excellent photocatalytic performance stability by maintaining over 90% in continuous five cycles (Fig. S8(a) in the ESM). After the cycling stability tests, the BCNNS photocatalyst was collected and characterized by TEM and XRD (Figs. S8(b) and S8(c) in the ESM), further verifying the structure stability of BCNNS.

Noteworthily, the detected H_2O_2 concentration is determined by the competition between formation (K_f) and decomposition (K_d) rate constant of H_2O_2 [3, 12]. The overall production kinetics of H_2O_2 ([H_2O_2]) can be determined by the following Eq. (3):

$$[H_2O_2] = (K_f/K_d) \times [1 - \exp(-K_d t)] \quad (1)$$

In our case, zero-order and first-order kinetics are adopted for estimation the formation and decomposition rate constants of H_2O_2, respectively [8]. The values of K_f and K_d of BCNNS, CNNS and commercial ZnO are evaluated via fitting the data of photocatalytic H_2O_2 formation (Fig. 3(d)) and decomposition (Fig. 3(e)) in 60 min by following Eqs. (2) and (3):

$$C_t = K_f t \quad (2)$$

$$\ln(C_0/C) = K_d t \quad (3)$$

The fitted $\ln(C_0/C)$-t plots are shown in Fig. S8(d) in the ESM, and the obtained date of K_f and K_d are displayed in Fig. 3(f). It is preferable for H_2O_2 production reaction with high K_f and low K_d values. According to the fitting results, BCNNS possesses a highest K_f value and relative lower K_d value, which can be ascribed to the controllable conduction and valence band levels, and improved adsorption and activation of O_2, leading to a significantly enhanced H_2O_2 production rate by BCNNS.

Furthermore, based on the binding strength between the adsorbed NH_3 and adsorption sites [35], the temperature programmed desorption of ammonia (NH_3-TPD) analysis was conducted to determine the influence of heteroatom (primarily B atoms)-doping on the formation of surface active sites. As revealed in Fig. 4(a). Since both the –NH_x and N–$(C)_3$ endow g-C_3N_4 with intrinsic Lewis basicity [36], no desorption peak can be observed

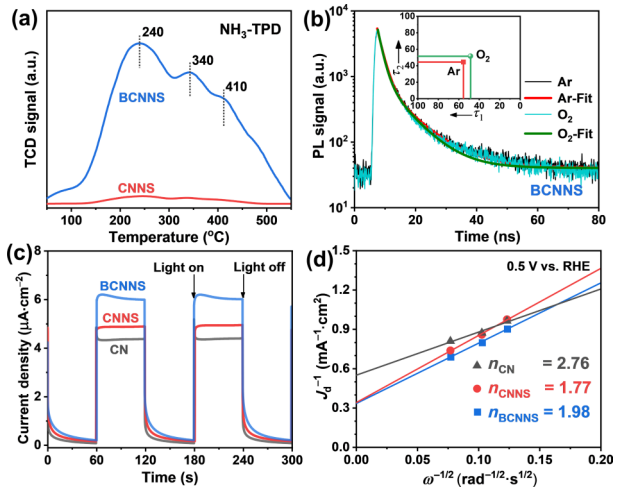

Figure 4 (a) NH_3-TPD profiles of CNNS and BCNNS. (b) Room-temperature TRPD spectra (excited by 375 nm) of BCNNS photocatalyst under different atmospheres. (c) Transient photocurrent responses and (d) K-L plots and corresponding electron transfer number (*n*) value of prepared samples.

in the NH_3-TPD profile of CNNS. For BCNNS sample, there are desorption broad peaks of around 240, 340 and 410 °C in the NH_3-TPD profile, corresponding to the presence of weak, moderate and strong acid sites, respectively [36–38]. The Lewis acid sites can be attributed to edge B–OH groups (weak acid sites), N_2BH (moderate acid sites) and BN_3 species (strong acid sites) [39, 40]. The superior Lewis acidity of B sites is mainly ascribed to the electron-deficient nature of B atoms, and meanwhile high electronegativity of adjacent N or O atoms that further attracts outer electrons from B atoms [40, 41]. The strong Lewis acidity enables the B–N units to be superior electron accepters, regulating the electron distribution of adjacent α-carbon atoms, and in turn to be active sites for ORR [42, 43].

The steady-state photoluminescence (PL) spectra and time-resolved photoluminescence decay (TRPD) spectra of prepared photocatalysts were applied to investigate the recombination of photogenerated charges and PL decay kinetics under different atmosphere, respectively. In Fig. S9(a) in the ESM, the CNNS exhibits a strong PL emission peak at 440 nm, higher than that of CN sample at ~450 nm. This is mainly due to the quantum confinement effect of thinner C_3N_4 layers in CNNS, contributing to a blue-shift of absorption edges and higher PL intensity [44, 45]. While after B-doping, BCNNS displays a dramatic PL quenching, indicating a significantly suppressed recombination of photogenerated charges, as a result of electron/holes redistribution driven by electron acceptors derived from introducing B–N units. The TRPD spectra of CNNS and BCNNS were further detected under different atmosphere (Ar or O_2). It can be drawn from Fig. S9(b) in the ESM that both lifetimes of photogenerated charge carries for BCNNS are obviously longer than that of CNNS, demonstrating an improved charge separation and transfer in B-doped carbon nitride [32, 46]. To observe the adsorption of O_2 on photocatalysts *in situ*, we replaced Ar atmosphere of PL decay with O_2 atmosphere. As expected, both of CNNS and BCNNS display remarkable decreased decay of emissive states in O_2 atmosphere than that recorded in Ar atmosphere, meaning efficient O_2 capture and interfacial electron transfer (Fig. S9(c) in the ESM and Fig. 4(b)) [47]. In addition, all TRPD curves can be well fitted through a bi-exponential function, as described in the supporting information [48, 49].

As revealed in Table S2 in the ESM, the determined short decay (radiative recombination) τ_1 (1.6 ns) and long decay (nonradiative recombination) τ_2 (7.6 ns) of BCNNS-O_2 are both lower than those of BCNNS-Ar (τ_1 = 1.9 ns, τ_2 = 9.2 ns), confirming an obviously decreased PL lifetime when detected in O_2 atmosphere. Furthermore, the determined average lifetime τ_{ave} of BCNNS-O_2 (6.6 ns) reduces for around 14% in Fig. 4(b), compared with that of BCNNS-Ar (7.7 ns). While τ_{ave} for CNNS sample only reduces 9% when detected in O_2 atmosphere (5 ns), rather than in Ar atmosphere (5.5 ns). In addition, as the A_1 and A_2 stand for the PL intensities (amplitudes) of the short and long decay components, the A_2 component for both CNNS and BCNNS are obviously increased under O_2 atmosphere, compared with that acquired from Ar atmosphere, reflecting an enhanced contribution of slow recombination (long decay) components to the overall lifetime of photoelectrons. The long decay of emissive states can be mainly ascribed to the nonradiative recombination of photoelectrons that trap in defects, vacancies, et al., or captured by surface reactants [47]. The significantly enhanced A_2 value of long decay (insets of Fig. S8(c) in the ESM and Fig. 4(b)) for BCNNS in O_2 declares the superior O_2 adsorption and activation, thereby contributing to the ORR.

The efficient separation and transfer of charge carries are essential for higher photocatalytic performance. Figure 4(c) shows the transient photocurrent curves of CN, CNNS and BCNNS photocatalyst electrodes under irradiation of 365 nm LED lamp (light intensity of 100 mW·cm^{-2}), revealing that the transient photocurrent density of BCNNS is obviously higher than that of CN and CNNS electrodes. Additionally, it can be detected obviously that a quick decreasing at the moment of light on occurred in the photocurrent curve of CN, which is mainly ascribed to rapid recombination of photogenerated charges [27]. Whereas photocurrent densities of both CNNS and BCNNS reached to a relative higher level, owing to their thinner nanosheet structure and B–N units induced electron donor-acceptor pairs [1, 26].

For an efficient photocatalytic H_2O_2 production pathway, the selectivity towards 2e$^-$ ORR is of great importance. Figures S10(a)–S10(c) in the ESM show the linear sweep voltammetry (LSV) curves of all prepared photocatalysts on rotating disk electrode (RDE) at different rotation speeds (in O_2-saturated 0.1 mol·L^{-1} KOH), demonstrating different disk current densities for CN, CNNS and BCNNS samples. Based on these polarization curves at different rotation speeds, the electron transfer numbers (*n*) were calculated through Koutecky-Levich (K-L) equations [51–54]. In Fig. 4(d), the calculated *n* value of BCNNS based on RDE measurement at 0.5 V vs. RHE achieves 1.98, almost equal to 2. While *n* values of CN and CNNS are estimated to be 2.76 and 1.77, respectively. This indicates that BCNNS exhibited more selective toward a 2-electron ORR pathway with dominating product of H_2O_2 [50].

To further verify the mechanism of such excellent 2e$^-$ ORR selectivity occurred on B–N units modified g-C_3N_4 at atomic scale, the density functional theory (DFT) calculations were conducted for O_2 adsorption and activation. The calculated optimal structure results indicate that O_2 has the lowest adsorption energy near the in-plane triazine ring of melon units (Fig. 5(a)). For pristine g-C_3N_4 melon units (CN), the O_2 molecules would preferentially adsorb at an adjacent C (d_{O-C}=1.50 Å) and N (d_{O-N}=1.45 Å) sites of CN heterocycle with adsorption energy (E_{ads}) of –0.47 eV (Fig. 5(a) left). After modified with B-doping, the BCN sample exhibits a more superior E_{ads} of –1.12 eV. As expected, O_2 molecules preferentially adsorb at B–N units sites of in-plane triazine ring (d_{O-B} = 1.54 Å and d_{O-N} = 1.44 Å), and meanwhile more electrons can be transferred to O=O (Δq = 0.69 e) as revealed in Fig. 5(a) right. The results indicate that O_2 molecules are more easily adsorbed on B–N units incorporated by B-doping, and the enhanced electron transfer is critical for subsequent proton-coupled electron transfer pathway for 2e$^-$ ORR [55]. Meaningfully,

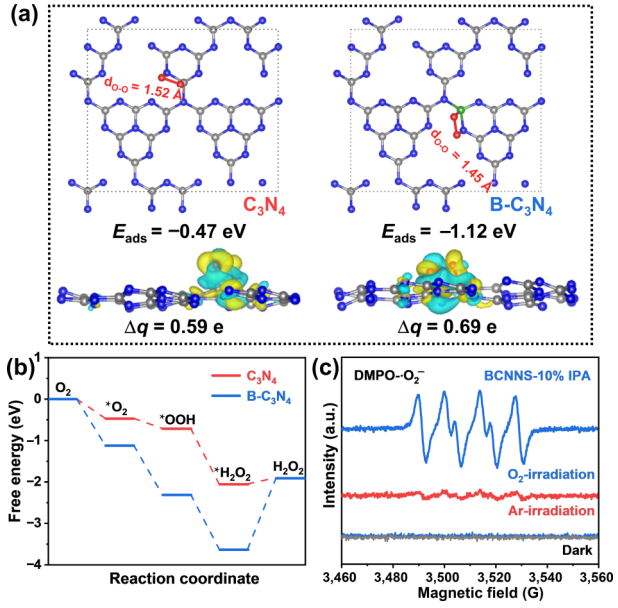

Figure 5 (a) Top and side views of the structure with different charge densities for O_2 adsorption on pristine g-C_3N_4 (left) and B-doped g-C_3N_4 (right). The yellow and light blue color represent the electron accumulation and electron dissipation area, respectively, and the isosurface value is 0.003 Å·e^{-3}. The grey, blue, green and red spheres represent C, N, B and O atoms, respectively. (b) Free energy diagrams of adsorbed O_2 reduction to H_2O_2 pathway. (c) DMPO-·O_2^- spin-trapping ESR spectra of BCNNS under different atmosphere and irradiation.

it can be found that the length of O=O bonds on BCN surface reduced obviously (d_{O-O} = 1.45 Å) than that on CN (d_{O-O} = 1.52 Å), demonstrating that the O–O band is easier to be broken with presence of B–N units [3].

Furthermore, according to previous reports, a reliable "side-on" binding configuration process (Figs. S11 and S12 in the ESM), and the free energy diagrams of disproportionation pathway of adsorbed O_2 molecules for H_2O_2 production were calculated in Fig. 5(b) [3, 55]. In this process, the *OOH is the crucial intermediate species, where the asterisk (*) represents the active site of prepared photocatalyst. Observably, the B–N units in BCN exhibits a much lower free energy for the activation and protonation of adsorbed O_2 molecules ($^*O_2$) to produce *OOH and $^*H_2O_2$ intermediates [4], following a PCET pathway to produce H_2O_2 [16], in favor of the H_2O_2 production activity.

Since the superoxide radicals (·O_2^-) intermediates is a powerful evidence for the presence of *OOH intermediates in a two-step single-electron O_2 reduction process [11, 50], we further collected *in situ* the 5,5-dimethyl-pyrroline N-oxide (DMPO) spin-trapping electron spin resonance (ESR) spectroscopy of prepared photocatalysts during photocatalytic H_2O_2 production [3]. In Fig. S12(a) of the ESM, characteristic signals assigned to DMPO-·O_2^- can be monitored for BCNNS and CNNS in 10% IPA under O_2 atmosphere after visible-light irradiation for 10 min, indicating that H_2O_2 is produced via two-step single-electron O_2 reduction (O_2+e$^-$ → ·O_2^- and ·O_2^-+2H$^+$+e$^-$ → H_2O_2) [1, 8]. Obviously, the intensities of DMPO-·O_2^- peaks for BCNNS are stronger than those of CNNS, demonstrating an improved H_2O_2-production activity [3]. Moreover, compared with that in Ar atmosphere, both of BCNNS and CNNS photocatalysts reveal enhanced intensities of DMPO-·O_2^- signals in O_2 (Figs. 5(c) and Fig. S12(b) in the ESM), further confirming that the H_2O_2 product is generated from gaseous O_2. Interestingly, the ESR spectroscopy of BCNNS tested in pure water only displays characteristic signals of DMPO-·OH (Fig. S12(c) in the ESM), indicating a good water oxidation ability. Nevertheless, there are undetectable amount of H_2O_2 produced by BCNNS or CNNS under irradiation in pure water. This further demonstrates that the produced H_2O_2 is exclusively generated from provided O_2, rather than oxidation of water [5].

3 Conclusions

To sum up, we have provided the first example of systematically studying the role of B–N units in C_3N_4 scaffolds on their performance in photocatalytic H_2O_2 production. Confirmed by characterizations, including phase and morphology structure analysis, optical/electrochemical tests, etc., the B–N units were embedded in carbon matrix to serve as electron acceptor, which can adjust the band structure of carbon nitride photocatalyst, accelerating the photogenerated charge transfer. Meanwhile, the electron-deficient B–N units can act as active sites for O_2 adsorption, in where local charge polarization is in favor of O_2 adsorption and subsequent selective 2e$^-$ ORR process with a H_2O_2 production rate of 1.16 mmol·L^{-1}·h^{-1} (2–5 times the performance of state-of-art metal free photocatalysts). BCNNS also provides an excellent stability by maintaining over 90% in continuous five cycles. The corresponding radical detection and DFT theoretical calculations were applied to further investigate and find strong evidence for the selective 2e$^-$ ORR pathway toward efficient H_2O_2 production, improved photocatalytic performance and stability, which can be ascribed to more delocalized charges of B–N bonds. This study would provide new insights into the nature of active site structure for H_2O_2 photosynthesis and development of high-efficiency catalyst for solar energy conversion.

Acknowledgements

This work was supported by the Jiangsu Provincial Double-Innovation Doctor Program (JSSCBS20210996).

Electronic Supplementary Material: Supplementary material (further details of the experimental section, SEM images, FTIR spectra, K-M plots, XPS valence band spectra, calibration curve for H_2O_2 detection, control experiments, cycling stability, PL spectra, TRPD spectra, RRDE tests, optimal structures with O_2 molecule toward H_2O_2 on B-doped g-C_3N_4, radical-trapping ESR spectra) is available in the online version of this article at https://doi.org/10.1007/s12274-022-4976-0.

References

[1] Yuan, L.; Zhang, C. Q.; Wang, J.; Liu, C.; Yu, C. Z. Mesoporous resin nanobowls with optimized donor-acceptor conjugation for highly efficient photocatalytic hydrogen peroxide production. *Nano Res.* **2021**, *14*, 3267–3273.

[2] Xia, C.; Xia, Y.; Zhu, P.; Fan, L.; Wang, H. T. Direct electrosynthesis of pure aqueous H_2O_2 solutions up to 20% by weight using a solid electrolyte. *Science* **2019**, *366*, 226–231.

[3] Chen, L.; Chen, C.; Yang, Z.; Li, S.; Chu, C. H.; Chen, B. L. Simultaneously tuning band structure and oxygen reduction pathway toward high-efficient photocatalytic hydrogen peroxide production using cyano-rich graphitic carbon nitride. *Adv. Funct. Mater.* **2021**, *31*, 2105731.

[4] Yang, Y.; Cheng, B.; Yu, J. G.; Wang, L. X.; Ho, W. TiO_2/In_2S_3 S-scheme photocatalyst with enhanced H_2O_2-production activity. *Nano Res.* , in press, DOI: 10.1007/s12274-021-3733-0.

[5] Chen, L.; Wang, L.; Wan, Y. Y.; Zhang, Y.; Qi, Z. M.; Wu, X. J.; Xu, H. X. Acetylene and diacetylene functionalized covalent triazine frameworks as metal-free photocatalysts for hydrogen peroxide production: A new two-electron water oxidation pathway. *Adv. Mater.* **2020**, *32*, 1904433.

[6] Huang, X.; Song, M.; Zhang, J.; Zhang, J. J.; Liu, W.; Zhang, C.; Zhang, W.; Wang, D. L. Investigation of MXenes as oxygen

reduction electrocatalyst for selective H_2O_2 generation. *Nano Res.* **2022**, *15*, 3927–3932.

[7] Gao, F.; He, J. Q.; Wang, H. W.; Lin, J. H.; Chen, R. X.; Yi, K.; Huang, F.; Lin, Z.; Wang, M. Y. Te-mediated electro-driven oxygen evolution reaction. *Nano Res. Energy* **2022**, 1: e9120028.

[8] Jiang, Z. C.; Zhang, Y.; Zhang, L. Y.; Cheng, B.; Wang, L. X. Effect of calcination temperatures on photocatalytic H_2O_2-production activity of ZnO nanorods. *Chinese J. Catal.* **2022**, *43*, 226–233.

[9] Teng, Z. Y.; Zhang, Q. T.; Yang, H. B.; Kato, K.; Yang, W. J.; Lu, Y. R.; Liu, S. X.; Wang, C. Y.; Yamakata, A.; Su, C. L. et al. Atomically dispersed antimony on carbon nitride for the artificial photosynthesis of hydrogen peroxide. *Nat. Catal.* **2021**, *4*, 374–384.

[10] Krishnaraj, C.; Sekhar Jena, H.; Bourda, L.; Laemont, A.; Pachfule, P.; Roeser, J.; Chandran, C. V.; Borgmans, S.; Rogge, S. M. J.; Leus, K. et al. Strongly reducing (Diarylamino)benzene-based covalent organic framework for metal-free visible light photocatalytic H_2O_2 generation. *J. Am. Chem. Soc.* **2020**, *142*, 20107–20116.

[11] Zhao, Y. J.; Liu, Y.; Wang, Z. Z.; Ma, Y. R.; Zhou, Y. J.; Shi, X. F.; Wu, Q. Y.; Wang, X.; Shao, M. W.; Huang, H. et al. Carbon nitride assisted 2D conductive metal-organic frameworks composite photocatalyst for efficient visible light-driven H_2O_2 production. *Appl. Catal. B* **2021**, *289*, 120035.

[12] Shi, H. Y.; Li, Y.; Wang, X. F.; Yu, H. G.; Yu, J. G. Selective modification of ultra-thin g-C_3N_4 nanosheets on the (110) facet of Au/$BiVO_4$ for boosting photocatalytic H_2O_2 production. *Appl. Catal. B* **2021**, *297*, 120414.

[13] Zhao, Y. B.; Zhang, P.; Yang, Z. C.; Li, L. N.; Gao, J. Y.; Chen, S.; Xie, T. F.; Diao, C. Z.; Xi, S. B.; Xiao, B. B. et al. Mechanistic analysis of multiple processes controlling solar-driven H_2O_2 synthesis using engineered polymeric carbon nitride. *Nat. Commun.* **2021**, *12*, 3701.

[14] Wang, L.; Lian, R.; Zhang, Y.; Ma, X. L.; Huang, J. W.; She, H. D.; Liu, C. L.; Wang, Q. Z. Rational preparation of cocoon-like g-C_3N_4/COF hybrids: Accelerated intramolecular charge delivery for photocatalytic hydrogen evolution. *Appl. Catal. B* **2022**, *315*, 121568.

[15] Wu, S.; Yu, H. T.; Chen, S.; Quan, X. Enhanced photocatalytic H_2O_2 production over carbon nitride by doping and defect engineering. *ACS Catal.* **2020**, *10*, 14380–14389.

[16] Moon, G. H.; Fujitsuka, M.; Kim, S.; Majima, T.; Wang, X. C.; Choi, W. Eco-friendly photochemical production of H_2O_2 through O_2 reduction over carbon nitride frameworks incorporated with multiple heteroelements. *ACS Catal.* **2017**, *7*, 2886–2895.

[17] Wang, X. Y.; Meng, J. Q.; Zhang, X. Y.; Liu, Y. Q.; Ren, M.; Yang, Y. X.; Guo, Y. H. Controllable approach to carbon-deficient and oxygen-doped graphitic carbon nitride: Robust photocatalyst against recalcitrant organic pollutants and the mechanism insight. *Adv. Funct. Mater.* **2021**, *31*, 2010763.

[18] Dai, Y. T.; Xiong, Y. J. Control of selectivity in organic synthesis via heterogeneous photocatalysis under visible light. *Nano Res. Energy* **2022**, 1: e9120006.

[19] Zhou, M.; Wang, S. B.; Yang, P. J.; Huang, C. J.; Wang, X. C. Boron carbon nitride semiconductors decorated with CdS nanoparticles for photocatalytic reduction of CO_2. *ACS Catal.* **2018**, *8*, 4928–4936.

[20] Shi, L.; Zhou, Z. B.; Zhang, Y. H.; Ling, C Y.; Li, Q.; Wang, J. L. Photocatalytic conversion of CO to fuels with water by B-doped graphene/g-C_3N_4 heterostructure. *Sci. Bull.* **2021**, *66*, 1186–1193.

[21] Wen, Y. K.; Zhuang, Z. C.; Zhu, H.; Hao, J. C.; Chu, K. B.; Lai, F. L.; Zong, W.; Wang, C.; Ma, P. M.; Dong, W. F. et al. Isolation of metalloid boron atoms in intermetallic carbide boosts the catalytic selectivity for electrocatalytic N_2 fixation. *Adv. Energy Mater.* **2021**, *11*, 2102138.

[22] Xia, Y.; Zhao, X. H.; Xia, C.; Wu, Z. Y.; Zhu, P.; Kim, J. Y.; Bai, X. W.; Gao, G. H.; Hu, Y. F.; Zhong, J. et al. Highly active and selective oxygen reduction to H_2O_2 on boron-doped carbon for high production rates. *Nat. Commun.* **2021**, *12*, 4225.

[23] Pang, S. T.; Wang, Z. Q.; Yuan, X. Y.; Pan, L. H.; Deng, W. Y.; Tang, H. B.; Wu, H. B.; Chen, S. S.; Duan, C. H.; Huang, F. et al. A facile synthesized polymer featuring B-N covalent bond and small singlet-triplet gap for high-performance organic solar cells. *Angew. Chem., Int. Ed.* **2021**, *60*, 8813–8817.

[24] Dou, C. D.; Long, X. J.; Ding, Z. C.; Xie, Z. Y.; Liu, J.; Wang, L. X. An electron-deficient building block based on the B←N unit: An electron acceptor for all-polymer solar cells. *Angew. Chem.* **2016**, *128*, 1458–1462.

[25] Wang, W. K.; Zhou, H. J.; Liu, Y. Y.; Zhang, S. B.; Zhang, Y. X.; Wang, G. Z.; Zhang, H. M.; Zhao, H. J. Formation of B-N-C coordination to stabilize the exposed active nitrogen atoms in g-C_3N_4 for dramatically enhanced photocatalytic ammonia synthesis performance. *Small* **2020**, *16*, 1906880.

[26] Luo, Z. S.; Fang, Y. X.; Zhou, M.; Wang, X. C. A borocarbonitride ceramic aerogel for photoredox catalysis. *Angew. Chem., Int. Ed.* **2019**, *58*, 6033–6037.

[27] Wang, J.; Wang, G. H.; Cheng, B.; Yu, J. G.; Fan, J. J. Sulfur-doped g-C_3N_4/TiO_2 S-scheme heterojunction photocatalyst for Congo Red photodegradation. *Chinese J. Catal.* **2021**, *42*, 56–68.

[28] Huang, C. J.; Chen, C.; Zhang, M. W.; Lin, L. H.; Ye, X. X.; Lin, S.; Antonietti, M.; Wang, X. C. Carbon-doped BN nanosheets for metal-free photoredox catalysis. *Nat. Commun.* **2015**, *6*, 7698.

[29] Jiang, W. J.; Ruan, Q. S.; Xie, J. J.; Chen, X. J.; Zhu, Y. F.; Tang, J. W. Oxygen-doped carbon nitride aerogel: A self-supported photocatalyst for solar-to-chemical energy conversion. *Appl. Catal. B* **2018**, *236*, 428–435.

[30] Hao, J. C.; Zhuang, Z. C.; Hao, J. C.; Wang, C.; Lu, S. L.; Duan, F.; Xu, F. P.; Du, M. L.; Zhu, H. Interatomic electronegativity offset dictates selectivity when catalyzing the CO_2 reduction reaction. *Adv. Energy Mater.* **2022**, *12*, 2200579.

[31] Wang, Y.; Li, H. R.; Yao, J.; Wang, X. C.; Antonietti, M. Synthesis of boron doped polymeric carbon nitride solids and their use as metal-free catalysts for aliphatic C-H bond oxidation. *Chem. Sci.* **2011**, *2*, 446–450.

[32] Zhao, D. M.; Wang, Y. Q.; Dong, C. L.; Huang, Y. C.; Chen, J.; Xue, F.; Shen, S. H.; Guo, L. J. Boron-doped nitrogen-deficient carbon nitride-based Z-scheme heterostructures for photocatalytic overall water splitting. *Nat. Energy* **2021**, *6*, 388–397.

[33] Wen, Y. K.; Zhu, H.; Hao, J. C.; Lu, S. L.; Zong, W.; Lai, F. L.; Ma, P. M.; Dong, W. F.; Liu, T. X.; Du, M. L. Metal-free boron and sulphur co-doped carbon nanofibers with optimized p-band centers for highly efficient nitrogen electroreduction to ammonia. *Appl. Catal. B* **2021**, *292*, 120144.

[34] Yang, Y. L.; Zhang, D. N.; Fan, J. J.; Liao, Y. L.; Xiang, Q. J. Construction of an ultrathin S-scheme heterojunction based on few-layer g-C_3N_4 and monolayer $Ti_3C_2T_x$ MXene for photocatalytic CO_2 reduction. *Sol. RRL* **2021**, *5*, 2000351.

[35] Ding, M. L.; Jiang, H. L. Incorporation of imidazolium-based poly(ionic liquid)s into a metal-organic framework for CO_2 capture and conversion. *ACS Catal.* **2018**, *8*, 3194–3201.

[36] Ran, Y.; Yu, X. L.; Liu, J. Q.; Cui, J. Y.; Wang, J. P.; Wang, L.; Zhang, Y. H.; Xiang, X.; Ye, J. H. Polymeric carbon nitride with frustrated Lewis pair sites for enhanced photofixation of nitrogen. *J. Mater. Chem. A* **2020**, *8*, 13292–13298.

[37] Zhao, J.; Lin, B. N.; Zhu, Y. F.; Zhou, Y. H.; Liu, H. Y. Phosphor-doped hexagonal boron nitride nanosheets as effective acid-base bifunctional catalysts for one-pot deacetalization-Knoevenagel cascade reactions. *Catal. Sci. Technol.* **2018**, *8*, 5900–5905.

[38] Zhuang, Z. C.; Li, Y. H.; Yu, R. H.; Xia, L. X.; Yang, J. R.; Lang, Z. Q.; Zhu, J. X.; Huang, J. Z.; Wang, J. O.; Wang, Y. et al. Reversely trapping atoms from a perovskite surface for high-performance and durable fuel cell cathodes. *Nat. Catal.* **2022**, *5*, 300–310.

[39] Liu, Z. K.; Yan, B.; Meng, S. Y.; Liu, R.; Lu, W. D.; Sheng, J.; Yi, Y. H.; Lu, A. H. Plasma tuning local environment of hexagonal boron nitride for oxidative dehydrogenation of propane. *Angew. Chem., Int. Ed.* **2021**, *60*, 19691–19695.

[40] Zhao, L. Y.; Dong, X. L.; Chen, J. Y.; Lu, A. H. A mechanochemical-assisted synthesis of boron, nitrogen Co-doped porous carbons as metal-free catalysts. *Chem. Eur. J.* **2020**, *26*, 2041–2050.

[41] Hao, J. C.; Zhuang, Z. C.; Cao, K. C.; Gao, G. H.; Wang, C.; Lai, F. L.; Lu, S. L.; Ma, P. M.; Dong, W. F.; Liu, T. X. et al. Unraveling the electronegativity-dominated intermediate adsorption on high-entropy alloy electrocatalysts. *Nat. Commun.* **2022**, *13*, 2662.

[42] Yang, Q. H.; Xu, W. W.; Gong, S.; Zheng, G. K.; Tian, Z. Q.; Wen,

Y. J.; Peng, L. M.; Zhang, L. J.; Lu, Z. Y.; Chen, L. Atomically dispersed Lewis acid sites boost 2-electron oxygen reduction activity of carbon-based catalysts. *Nat. Commun.* **2020**, *11*, 5478.

[43] Lu, Z. Y.; Chen, G. X.; Siahrostami, S.; Chen, Z. H.; Liu, K.; Xie, J.; Liao, L.; Wu, T.; Lin, D. C.; Liu, Y. Y. et al. High-efficiency oxygen reduction to hydrogen peroxide catalysed by oxidized carbon materials. *Nat. Catal.* **2018**, *1*, 156–162.

[44] Niu, P.; Zhang, L. L.; Liu, G.; Cheng, H. M. Graphene-like carbon nitride nanosheets for improved photocatalytic activities. *Adv. Funct. Mater.* **2012**, *22*, 4763–4770.

[45] Sun, X. H.; Sun, L.; Li, G. N.; Tuo, Y.; Ye, C. L.; Yang, J. R.; Low, J.; Yu, X.; Bitter, J. H.; Lei, Y. P. et al. Phosphorus tailors the *d*-band center of copper atomic sites for efficient CO_2 photoreduction under visible-light irradiation. *Angew. Chem. , Int. Ed.* , in press, DOI: 10.1002/anie.202207677.

[46] Chen, Y. L.; Liu, X. Q.; Hou, L.; Guo, X. R.; Fu, R. W.; Sun, J. M. Construction of covalent bonding oxygen-doped carbon nitride/graphitic carbon nitride Z-scheme heterojunction for enhanced visible-light-driven H_2 evolution. *Chem. Eng. J.* **2020**, *383*, 123132.

[47] Li, H.; Shang, J.; Ai, Z. H.; Zhang, L. Z. Efficient visible light nitrogen fixation with BiOBr nanosheets of oxygen vacancies on the exposed {001} facets. *J. Am. Chem. Soc.* **2015**, *137*, 6393–6399.

[48] Wang, W. K.; Zhang, H. M.; Zhang, S. B.; Liu, Y. Y.; Wang, G. Z.; Sun, C. H.; Zhao, H. J. Potassium-ion-assisted regeneration of active cyano groups in carbon nitride nanoribbons: Visible-light-driven photocatalytic nitrogen reduction. *Angew. Chem., Int. Ed.* **2019**, *58*, 16644–16650.

[49] Sayed, M.; Xu, F. Y.; Kuang, P. Y.; Low, J.; Wang, S. Y.; Zhang, L. Y.; Yu, J. G. Sustained CO_2-photoreduction activity and high selectivity over Mn, C-codoped ZnO core-triple shell hollow spheres. *Nat. Commun.* **2021**, *12*, 4936.

[50] Zhao, Y. J.; Liu, Y.; Cao, J. J.; Wang, H.; Shao, M. W.; Huang, H.; Liu, Y.; Kang, Z. H. Efficient production of H_2O_2 via two-channel pathway over ZIF-8/C_3N_4 composite photocatalyst without any sacrificial agent. *Appl. Catal. B* **2020**, *278*, 119289.

[51] Jing, H. Y.; Zhu, P.; Zheng, X. B.; Zhang, Z. D.; Wang, D. S.; Li, Y. D. Theory-oriented screening and discovery of advanced energy transformation materials in electrocatalysis. *Adv. Powder Mater.* **2022**, *1*, 100013.

[52] Zhuang, Z. C.; Li, Y.; Li, Y. H.; Huang, J. Z.; Wei, B.; Sun, R.; Ren, Y. J.; Ding, J.; Zhu, J. X.; Lang, Z. Q. et al. Atomically dispersed nonmagnetic electron traps improve oxygen reduction activity of perovskite oxides. *Energy Environ. Sci.* **2021**, *14*, 1016–1028.

[53] Ji, M. W.; Yang, X.; Chang, S. D.; Chen, W. X.; Wang, J.; He, D. S.; Hu, Y.; Deng, Q.; Sun, Y.; Li, B. et al. RuO_2 clusters derived from bulk $SrRuO_3$: Robust catalyst for oxygen evolution reaction in acid. *Nano Res.* **2022**, *15*, 1959–1965.

[54] Guo, F. J.; Zhang, M. Y.; Yi, S. C.; Li, X. X.; Xin, R.; Yang, M.; Liu, B.; Chen, H. B.; Li, H. M.; Liu, Y. J. Metal-coordinated porous polydopamine nanospheres derived Fe_3N-FeCo encapsulated N-doped carbon as a highly efficient electrocatalyst for oxygen reduction reaction. *Nano Res. Energy* **2022**, 1: e9120027.

[55] Zhang, P.; Tong, Y. W.; Liu, Y.; Vequizo, J. J. M.; Sun, H. W.; Yang, C.; Yamakata, A.; Fan, F. T.; Lin, W.; Wang, X. C. et al. Heteroatom dopants promote two-electron O_2 reduction for photocatalytic production of H_2O_2 on polymeric carbon nitride. *Angew. Chem., Int. Ed.* **2020**, *59*, 16209–16217.